

# Band-edge engineering for controlled multi-modal nanolasing in plasmonic superlattices

Danqing Wang<sup>1</sup>, Ankun Yang<sup>2†</sup>, Weijia Wang<sup>1</sup>, Yi Hua<sup>2</sup>, Richard D. Schaller<sup>3,4</sup>, George C. Schatz<sup>1,3\*</sup> and Teri W. Odom<sup>1,2,3\*</sup>

**Single band-edge states can trap light and function as high-quality optical feedback for microscale lasers and nanolasers. However, access to more than a single band-edge mode for nanolasing has not been possible because of limited cavity designs. Here, we describe how plasmonic superlattices—finite-arrays of nanoparticles (patches) grouped into microscale arrays—can support multiple band-edge modes capable of multi-modal nanolasing at programmed emission wavelengths and with large mode spacings. Different lasing modes show distinct input-output light behaviour and decay dynamics that can be tailored by nanoparticle size. By modelling the superlattice nanolasers with a four-level gain system and a time-domain approach, we reveal that the accumulation of population inversion at plasmonic hot spots can be spatially modulated by the diffractive coupling order of the patches. Moreover, we show that symmetry-broken superlattices can sustain switchable nanolasing between a single mode and multiple modes.**

Engineering electronic and photonic band structures can lead to controlled emission wavelengths and output efficiencies of semiconductor materials and optical devices<sup>1–3</sup>. Slow light trapped at band-edge states can support standing waves that have also functioned as high-quality optical feedback for lasing from photonic bandgap crystals<sup>4,5</sup>, metal–dielectric waveguides<sup>6</sup> and metal nanoparticle arrays<sup>7–10</sup>. Compared with semiconducting lasers, plasmon nanolasers can support ultrasmall mode volumes that can beat the diffraction limit by exploiting localized surface plasmons from single nanoparticles (NPs)<sup>11–13</sup> and surface plasmon polaritons on metal films<sup>14,15</sup>; however, most cavity architectures suffer from large radiative losses and lack beam directionality. Moreover, unwanted multi-modal nanolasing from plasmonic lasers exhibits both uncontrolled mode spacing and output behaviour<sup>14–17</sup>.

Different from periodic dielectric structures that support both upper and lower band edges in distributed feedback lasers<sup>18</sup>, periodic metal NP arrays in a homogeneous dielectric environment exhibit only single band-edge lattice plasmons that are characterized by suppressed radiative loss and subwavelength localized field enhancement around the NPs<sup>19–21</sup>. Recently, we discovered that high-quality band-edge lattice plasmons (quality factor  $Q > 200$ ) can contribute to single-mode lasing at room temperature with directional emission and lasing wavelengths that can be tuned in real time<sup>7,9</sup>. To achieve multiplexing, multiple optical frequencies with well-defined and separated spacings are needed to increase storage capability and facilitate optical processing<sup>22–24</sup>.

Here, we show how plasmonic NP superlattices enable access to multiple band-edges at zero and non-zero wavevectors that can be exploited for multi-modal lasing with characteristics distinct from traditional photonic and plasmonic lasers. Compared with multi-modal lasing that usually lacks tunability, superlattice plasmons can achieve accurate control over the wavelength and spectral separation of multiple lasing modes. Moreover, tuning NP size can provide an additional degree of freedom for manipulating the output behaviour of different lasing modes. As a result of symmetry

breaking of the NP superlattice, dynamically switchable lasing between single and multiple modes was achieved. Our modelling of multi-modal lasing based on a four-level gain system and a time-domain approach not only showed excellent agreement with experiments but also revealed that the switchable lasing can be attributed to the spatial distribution of population inversion at dipolar plasmonic hot spots.

## Lasing emission from superlattice nanoparticle arrays

Figure 1 compares the linear optical properties and lasing emission from gold NP superlattices and single-lattice NP arrays. The NPs were supported on substrates of fused silica (refractive index  $n = 1.48$ ) and liquid gain superstrates of IR-140 dye in dimethyl sulfoxide (DMSO,  $n = 1.46$ ) to achieve the highest-quality lattice plasmon modes (Methods). Superlattices with NP spacing  $a_0 = 600$  nm and patch periodicity  $A_0 = 24$   $\mu\text{m}$  were fabricated over centimetre-squared areas by multiscale nanofabrication tools that combine contact and phase-shifting photolithography<sup>25,26</sup> (Fig. 1a).  $A_0$  was selected such that the gain emission (centred at 860 nm, orange curve) overlapped with different high-order superlattice (SL) plasmons  $\lambda_{\text{SL}}^{\text{a}} = 864$  nm and  $\lambda_{\text{SL}}^{\text{c1}} = 881$  nm (blue curve), as determined by coupling of single-patch lattice plasmons and Bragg modes ( $\lambda_{\text{SL}}^{\text{a}}$  and  $\lambda_{\text{SL}}^{\text{c1}}$  would be  $\lambda_{\text{SL}}^{40}$  and  $\lambda_{\text{SL}}^{39}$  for  $A_0 = 24$   $\mu\text{m}$  according to indexing based on diffractive coupling)<sup>26</sup>.  $\lambda_{\text{SL}}^{\text{a}}$  exhibited the same resonance wavelength and in-phase oscillations between NPs as that of the single band-edge lattice plasmon mode  $\lambda_{\text{L}}$  in a single-lattice array, although the full-width at half-maximum (FWHM) of the dip was larger (Fig. 1b). The additional mode at  $\lambda_{\text{SL}}^{\text{c1}}$  showed overall single-period phase oscillations between adjacent NPs within a single patch because of patch–patch coupling (Supplementary Fig. 1).

Consistent with previous work<sup>7,9</sup>, the high-quality band-edge lattice plasmon at  $\lambda_{\text{L}}$  contributed to a single lasing mode at  $\lambda_{\text{L}}^{\text{I}} = 862$  nm with directional emission and an extremely narrow linewidth (FWHM = 0.3 nm). In contrast, multiple lasing peaks at  $\lambda_{\text{SL}}^{\text{I}} = 863$  nm,  $\lambda_{\text{SL}}^{\text{II}} = 874$  nm and  $\lambda_{\text{SL}}^{\text{III}} = 884$  nm were observed in

<sup>1</sup>Graduate Program in Applied Physics, Northwestern University, Evanston, Illinois 60208, USA. <sup>2</sup>Department of Materials Science and Engineering, Northwestern University, Evanston, Illinois 60208, USA. <sup>3</sup>Department of Chemistry, Northwestern University, Evanston, Illinois 60208, USA. <sup>4</sup>Center for Nanoscale Materials, Argonne National Laboratory, Argonne, Illinois 60439, USA. <sup>†</sup>Present address: Department of Materials Science and Engineering, Stanford University, Stanford, California 94305, USA. \*e-mail: g-schatz@northwestern.edu; todom@northwestern.edu

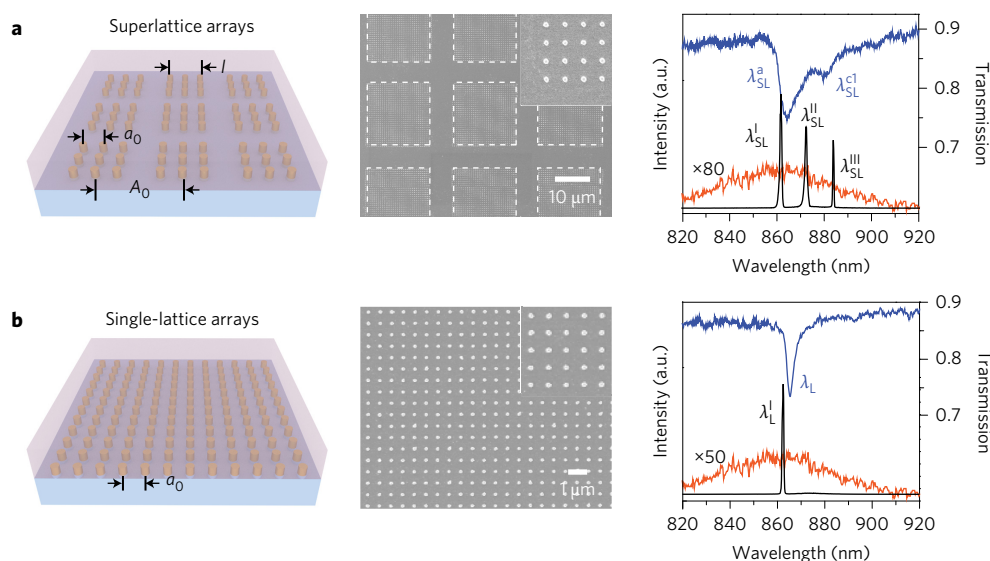


**Figure 1 | Multi-modal nanolasing in gold nanoparticle superlattices surrounded by liquid dye solutions.** **a**, Schematic (left), scanning electron microscopy (SEM) image (middle) and measured lasing emission (right) from NP superlattices with NP spacing  $a_0 = 600$  nm, NP diameter  $d = 120$  nm, height  $h = 50$  nm, patch side length  $l = 18$   $\mu\text{m}$  and patch periodicity  $A_0 = 24$   $\mu\text{m}$  embedded in IR-140-DMSO (concentration  $C = 0.6$  mM). **b**, Same as **a**, but for single-lattice arrays with the same NP diameter  $d = 120$  nm, height  $h = 50$  nm and spacing  $a_0 = 600$  nm. IR-140-DMSO superstrates surrounding single-lattice and superlattice NP arrays were pumped with an 800-nm femtosecond-pulsed laser, and light was collected normal to the sample surface (Methods and Supplementary Fig. 2). FWHM of lattice plasmon resonances is 6.2 nm at  $\lambda_{\text{SL}}^{\text{a}}$  and 4.2 nm at  $\lambda_{\text{L}}$  (right). In the schematics (left), the IR-140-DMSO gain media is shown in pink. For the measured lasing emission (right), linear optical properties are in blue, dye emission is in orange with intensity rescaled, and lasing emission is in black.

superlattices with large modal spacing ( $\Delta\lambda = 10\text{--}11$  nm) and narrow spectral linewidths (FWHM  $< 0.5$  nm). The lasing mode  $\lambda_{\text{SL}}^{\text{l}}$  originated from the SL plasmon mode  $\lambda_{\text{SL}}^{\text{a}}$ , similar to how the wavelength of the band-edge lattice plasmon mode  $\lambda_{\text{L}}$  in single-lattice NP arrays determined the lasing wavelength  $\lambda_{\text{L}}^{\text{l}}$  (refs 25,26).  $\lambda_{\text{SL}}^{\text{ii}}$  and  $\lambda_{\text{SL}}^{\text{cl}}$  were new lasing modes that can uniquely be attributed to patch–patch coupling.  $\lambda_{\text{SL}}^{\text{iii}}$  can be correlated with the SL plasmon at  $\lambda_{\text{SL}}^{\text{a}}$  based on good spectral overlap and emission position, but surprisingly,  $\lambda_{\text{SL}}^{\text{ii}}$  was absent in the transmission spectrum even though lasing emission at that wavelength was evident.

### Multi-modal superlattice lasing at band-edge modes

To understand the origin of the different lasing modes, we first determined the optical band structure of NP superlattices by stitching together zero-order angle-resolved transmission spectra (Methods). Compared with the single band-edge state at  $\lambda_{\text{L}}$  in single-lattice NP arrays (located at in-plane wavevector  $k_{\parallel} = 0$ ), multiple band-edge modes were observed under transverse electric (TE) polarization in NP superlattices not only at  $k_{\parallel} = 0$  ( $\lambda_{\text{SL}}^{\text{a}}, \lambda_{\text{SL}}^{\text{cl}}$ ), but also at  $k_{\parallel} = \pm 0.13, \pm 0.26$  and  $\pm 0.39$   $\mu\text{m}^{-1}$  ( $\lambda_{\text{SL}}^{\text{b1}}, \lambda_{\text{SL}}^{\text{c2}}, \lambda_{\text{SL}}^{\text{b2}}$ ) (Fig. 2a). Band-edge modes at both zero and non-zero  $k_{\parallel}$  arose from coupling of localized surface plasmons of the NPs to different diffraction modes from the hierarchical structure ( $A_0$ ). Based on finite-difference time-domain (FDTD) methods, simulated band structures showed excellent agreement with measurements (Supplementary Fig. 3).

We indexed different Bragg modes of the superlattice as  $[k_x k_y k'_x k'_y]$  in reciprocal space, where  $k_x$  ( $k_y$ ) and  $k'_x$  ( $k'_y$ ) denoted grating vectors from the NP ( $k = 2\pi/a_0$ ) and patch spacing ( $k' = 2\pi/A_0$ ) (Supplementary Fig. 4). At  $\lambda_{\text{SL}}^{\text{a}}$  ( $k_{\parallel} = 0$ ), two propagating Bragg modes  $[1000]$  and  $[1\bar{0}00]$  with opposite wavevectors formed a standing wave. At  $\lambda_{\text{SL}}^{\text{b1}}$  ( $k_{\parallel} = \pm 0.13$   $\mu\text{m}^{-1}$ ), an overall  $0.5k'_x$  from two coupled Bragg modes  $[1000]$  and  $[10\bar{1}0]$  compensated for non-zero  $k_{\parallel}$ . Therefore, plasmonic NP superlattices can exhibit standing-wave modes with very low group velocities ( $v_g = \delta\omega/\delta k_{\parallel}$ , where  $\omega$  is the angular frequency) at all band edges at  $\lambda_{\text{SL}}^{\text{a}}, \lambda_{\text{SL}}^{\text{b1}}, \lambda_{\text{SL}}^{\text{b2}}, \lambda_{\text{SL}}^{\text{cl}}, \lambda_{\text{SL}}^{\text{c2}}$ . The electric field enhancement was localized within the subwavelength vicinity of the NPs, where the fields

oscillated with nearly the same phase and amplitude (Fig. 2b and Supplementary Fig. 4). Band-edge modes at  $k_{\parallel} \neq 0$  only exist for plasmonic NP superlattices and are not observed for dielectric NPs because of weak near-field coupling between patches in the visible and near-infrared regions (Supplementary Figs 5 and 6).

Side-by-side comparison of an angle-resolved lasing emission map and band structure revealed that superlattice lasing modes had a one-to-one correspondence with the band-edge modes (Fig. 2c). For single-lattice arrays, a single lasing mode appeared at the  $k_{\parallel} = 0$  band edge, and in the emission map, a single lasing point was observed at the detection angle  $\theta_D = 0^\circ$ , normal to the NP arrays (Supplementary Fig. 7). In contrast, for NP superlattices, lasing action at  $\lambda_{\text{SL}}^{\text{l}}$  and  $\lambda_{\text{SL}}^{\text{iii}}$  (from band edges at  $\lambda_{\text{SL}}^{\text{a}}$  and  $\lambda_{\text{SL}}^{\text{cl}}$ , respectively) emerged at  $\theta_D = 0^\circ$ , while  $\lambda_{\text{SL}}^{\text{ii}}$  matched well with band edges at  $k_{\parallel} \neq 0$ , which suggests that standing waves at both zero and non-zero  $k_{\parallel}$  can support lasing action. Although the band edge at  $\lambda_{\text{SL}}^{\text{b2}}$  was barely resolved in the measured band structure, lasing action at  $\lambda_{\text{SL}}^{\text{ii}}$  was still observed in the emission map, which indicates how lasing could serve as a probe to identify band-edge points with a high local density of optical states.

Plasmonic superlattice lasers also exhibit distinct spatial coherence characteristics (Methods). Besides the central, single spot at  $\theta_D = 0^\circ$  similar to single-lattice NP arrays, multiple satellite spots appeared on each side of the central beam (at  $\theta_D = \pm 1.04^\circ$  and  $\pm 2.08^\circ$ ) (Fig. 2d). The angular correlation between band structure and the angle-resolved emission map along  $x$  (Fig. 2c) identified that lasing at  $\lambda_{\text{SL}}^{\text{l}}$  and  $\lambda_{\text{SL}}^{\text{iii}}$  appeared at  $\theta_D = 0^\circ$  and  $\pm 2.08^\circ$ , while  $\lambda_{\text{SL}}^{\text{ii}}$  contributed to the left and right satellite beams at  $\theta_D = \pm 1.04^\circ$ . The emission map acquired by sweeping  $\theta_D$  along  $y$  verified that under TE polarization, the multiple spots along  $y$  resulted from diffractive effects of patch–patch interactions, and the alternating of different lasing wavelengths among spots only appeared along  $x$  (Supplementary Fig. 8). All emission beams exhibited only minor beam divergence ( $< 1^\circ$ ), which in combination with the narrow spectral linewidth ( $< 0.5$  nm) supports the coherence of each lasing mode.

To understand the real-time lasing build-up from plasmonic NP superlattices, we combined the FDTD method with a four-level

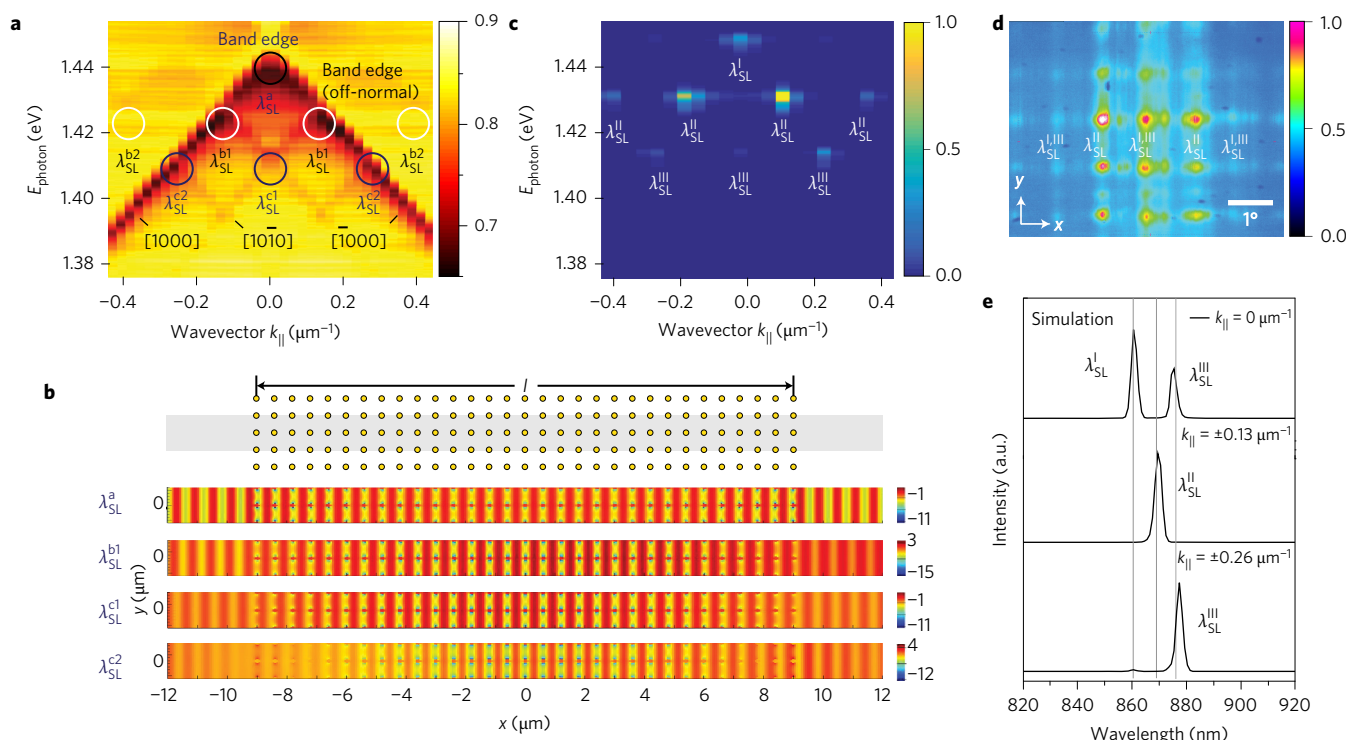


**Figure 2 | Experiments and simulations of band-edge modes at zero and non-zero wavevectors supporting standing waves for multi-modal nanolasing.**

**a**, Measured band structure of two-dimensional (2D) superlattice arrays. **b**, Simulated near-field distributions  $E_y$  of multiple band-edges within plotted area of  $24 \times 1.2 \mu\text{m}$  (top) in the middle of 2D superlattices. **c**, Measured angle-resolved emission of multi-modal lasing, with emission signals collected within  $\pm 3.5^\circ$  relative to the sample surface normal. The raw data of angle-resolved lasing spectra can be found in Supplementary Fig. 7. **d**, Satellite spots around a central spot were detected in the far-field beam profile, where the centre represented  $\theta_D = 0^\circ$  along  $x$  and  $y$ . **e**, Lasing spectra from band edges at  $k_{\parallel} = 0$  (top),  $k_{\parallel} = \pm 0.13 \mu\text{m}^{-1}$  (middle) and  $k_{\parallel} = \pm 0.26 \mu\text{m}^{-1}$  (bottom) by FDTD simulations. All results under TE polarization. Scale bar in **a** indicates transmission intensity, increasing from black to white, and those in **b** and **c** indicate normalized emitted photon intensity, increasing from blue to yellow or red.

one-electron system of dye molecules subject to the Pauli exclusion principle (Methods and Supplementary Fig. 9). FDTD simulations with the Pauli exclusion principle showed lasing action in single-lattice arrays comparable to that of our previous method<sup>7</sup> that did not consider electron spin; only a minor change of oscillation amplitude in the time-dependent population inversion was observed (Supplementary Fig. 10). Pumping of the ground electronic state resulted in lasing modes at  $\lambda_{\text{SL}}^{\text{I}}$  and  $\lambda_{\text{SL}}^{\text{III}}$  for  $k_{\parallel} = 0$  with wavelengths that can be correlated with SL plasmons  $\lambda_{\text{SL}}^{\text{a}} + \lambda_{\text{SL}}^{\text{c1}}$  and  $\lambda_{\text{SL}}^{\text{c2}}$  (Supplementary Fig. 11). Note that the output spectrum only showed two lasing modes  $\lambda_{\text{SL}}^{\text{I}}$  and  $\lambda_{\text{SL}}^{\text{III}}$  at  $k_{\parallel} = 0$  and could not reveal  $\lambda_{\text{SL}}^{\text{II}}$  because this time-domain approach cannot represent SL plasmons at different  $k_{\parallel}$  simultaneously. However, simulations with a plane-wave incident at  $\theta_i = \pm 1.04^\circ$  and  $\pm 2.08^\circ$  could produce lasing at  $\lambda_{\text{SL}}^{\text{II}}$  (from  $\lambda_{\text{SL}}^{\text{b1}}$  at  $k_{\parallel} = \pm 0.13 \mu\text{m}^{-1}$ ) and  $\lambda_{\text{SL}}^{\text{III}}$  (from  $\lambda_{\text{SL}}^{\text{c1}}$  at  $k_{\parallel} = \pm 0.26 \mu\text{m}^{-1}$ ) by introducing a phase shift at the micro-scale unit-cell boundary (Fig. 2e). Modelling of lasing action from large-unit-cell lattices (tens of micrometres) and at non-zero  $k_{\parallel}$  was not possible in our previous home-built FDTD codes because of computational efficiency<sup>7,9</sup>.

### Output behaviour of superlattice lasing modes

Mode competition is common in semiconductor lasers, where multiple cavity modes compete for available gain; hence, oscillations in one mode generally reduce and suppress gain for others<sup>27</sup>. Distinct from traditional systems, plasmonic NP superlattices can support multiple lasing modes simultaneously because of a combination of factors: (i) the large gain bandwidth of the dye ( $\sim 50 \text{ nm}$ ); (ii) the short pulsed laser excitation ( $\sim 90 \text{ fs}$ ) that avoids accumulation of mode competition over limited photon travelling cycles; (iii) widely separated spectral resonances of SL plasmons ( $\sim 10 \text{ nm}$ ); and

(iv) different near-field spatial overlap of SL modes (Supplementary Fig. 1) with the gain media<sup>27</sup>. Since all band-edge wavelengths for this particular NP superlattice ( $A_0 = 24 \mu\text{m}$ ;  $l = 18 \mu\text{m}$ )— $\lambda_{\text{SL}}^{\text{a}}$ ,  $\lambda_{\text{SL}}^{\text{b1}}$ ,  $\lambda_{\text{SL}}^{\text{b2}}$ ,  $\lambda_{\text{SL}}^{\text{c1}}$ ,  $\lambda_{\text{SL}}^{\text{c2}}$ —were within the gain envelope, multi-modal lasing could exist and be captured simultaneously by a single detector (collection angle around  $3^\circ$ ).

At low pump powers,  $\lambda_{\text{SL}}^{\text{II}}$  at  $k_{\parallel} \neq 0$  and  $\lambda_{\text{SL}}^{\text{III}}$  at  $k_{\parallel} = 0$  emerged with lasing thresholds lower than  $\lambda_{\text{SL}}^{\text{I}}$  (Fig. 3a and Supplementary Movie 1). Interestingly,  $\lambda_{\text{SL}}^{\text{I}}$  surpassed  $\lambda_{\text{SL}}^{\text{III}}$  at  $0.35 \text{ mJ cm}^{-2}$  and continued to increase, while  $\lambda_{\text{SL}}^{\text{II}}$  and  $\lambda_{\text{SL}}^{\text{III}}$  saturated at high pump fluence (Fig. 3b,c); these trends were similar for all NP superlattices tested (Supplementary Fig. 12). In FDTD modelling at  $k_{\parallel} = 0$ , we also observed an early rise of  $\lambda_{\text{SL}}^{\text{III}}$  but dominant growth of  $\lambda_{\text{SL}}^{\text{I}}$  at high pump power (Fig. 3c and Supplementary Fig. 13). These power-dependent output behaviours may be attributed to the near-field enhancement of SL plasmons and their mode quality  $Q (= \frac{\lambda}{\Delta\lambda})$ , where  $\lambda$  represents the resonance wavelength and  $\Delta\lambda$  the linewidth).  $Q_{\lambda_{\text{SL}}^{\text{c1}}} = 197$  is slightly larger than  $Q_{\lambda_{\text{SL}}^{\text{a}}} = 139$ , which suggests that photons from  $\lambda_{\text{SL}}^{\text{c1}}$  are trapped within the cavity for more cycles than  $\lambda_{\text{SL}}^{\text{a}}$  such that there is more available gain at  $\lambda_{\text{SL}}^{\text{c1}}$  at low pump powers (Supplementary Fig. 14). Thus, lasing action was first observed at  $\lambda_{\text{SL}}^{\text{II}}$  and  $\lambda_{\text{SL}}^{\text{III}}$  (from band edges at  $\lambda_{\text{SL}}^{\text{b1}}$ ,  $\lambda_{\text{SL}}^{\text{b2}}$ ,  $\lambda_{\text{SL}}^{\text{c1}}$  and  $\lambda_{\text{SL}}^{\text{c2}}$ ). At high pump powers,  $\lambda_{\text{SL}}^{\text{I}}$  dominated since the mode at  $\lambda_{\text{SL}}^{\text{a}}$  exhibited a seven-fold stronger local field that enhanced the stimulated emission term in the rate equations (Supplementary Fig. 9b).

Unlike existing photonics and plasmonic lasers that exhibit fixed intensity ratios across the different modes<sup>28</sup> or a single, dominant mode with increased pump power<sup>15</sup>, the output behaviour of SL plasmon lasing peaks can be uniquely controlled by manipulating the near-field intensity of the individual modes. For example, by increasing NP size from  $d = 120 \text{ nm}$  to  $d = 125 \text{ nm}$

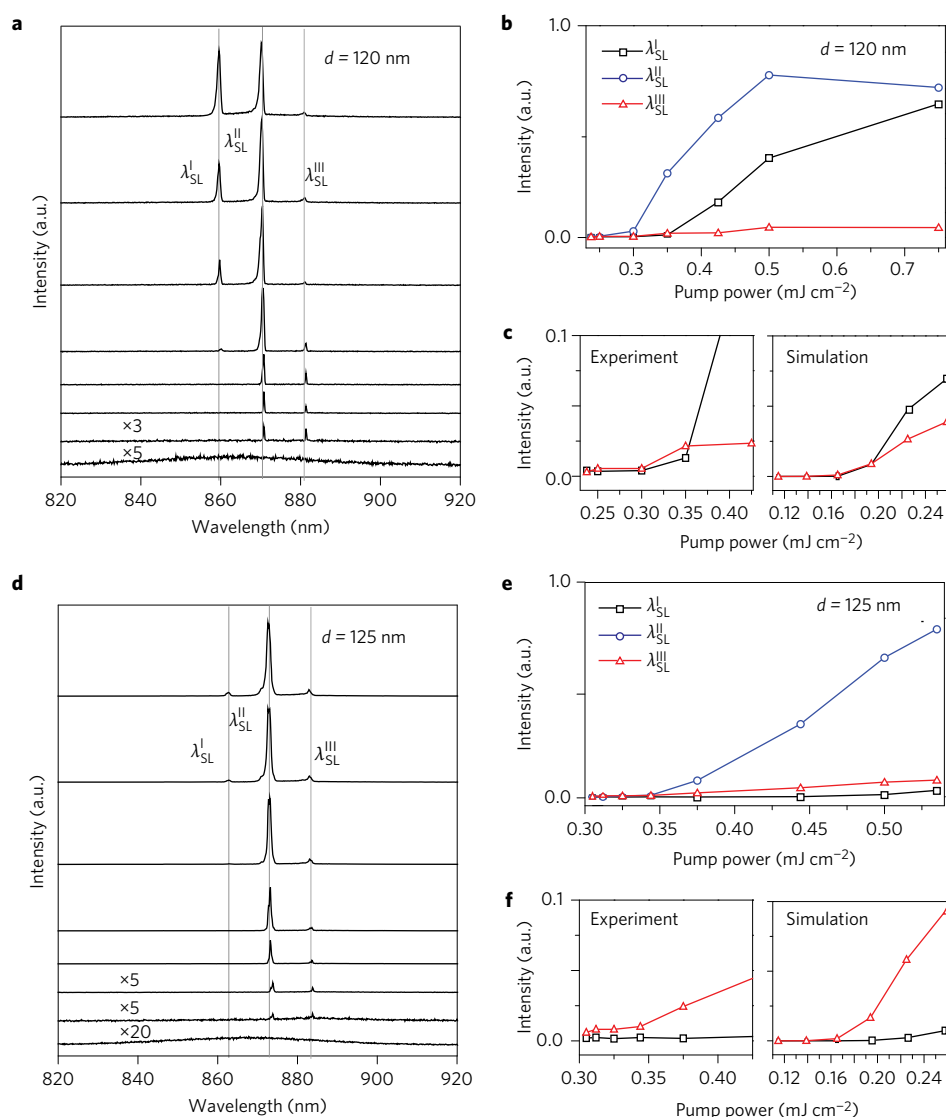


**Figure 3 | Multi-modal nanolasing from plasmonic superlattices with controlled output behaviours and spatial coherence.** **a**, Measured output profiles of multi-modal lasing with dye concentration and increased pump power at  $0.2\text{--}0.8\text{ mJ cm}^{-2}$  for 2D superlattices with  $d = 120$  nm. **b**, Experimental threshold curve of multi-modal lasing with  $d = 120$  nm. **c**, Experimental (left) and simulated (right) output behaviours of  $\lambda_{SL}^I$  and  $\lambda_{SL}^{III}$  with  $d = 120$  nm. Experimental data are a zoom-in of **b**. **d**, Output profiles of larger NP size  $d = 125$  nm with increased pump power at  $0.3\text{--}0.6\text{ mJ cm}^{-2}$ . Intensities are rescaled at low pump powers in **a** and **d**. **e**, Experimental threshold curve of multi-modal lasing with  $d = 125$  nm. **f**, Experimental (left) and simulated (right) output behaviours of  $\lambda_{SL}^I$  and  $\lambda_{SL}^{III}$  with  $d = 125$  nm. Experimental data are a zoom-in of **e**. Full pump power range of simulated data for **c** and **f** can be found in Supplementary Fig. 13.  $C = 0.63\text{ mM}$  for both superlattice lasers.

(Fig. 3d), all band-edge modes red-shifted and those at longer wavelengths had higher intensity (Supplementary Fig. 15). The stronger local **E** field at  $\lambda_{SL}^{c1}$  led to stronger stimulated emission at  $\lambda_{SL}^{III}$ ; thus,  $\lambda_{SL}^{II}$  and  $\lambda_{SL}^{III}$  showed a dominant increase at high pump powers while  $\lambda_{SL}^I$  remained relatively weak and did not surpass  $\lambda_{SL}^{III}$  in simulation or experiment (Fig. 3e,f and Supplementary Movie 2). Note that  $\lambda_{SL}^{II}$  was located closer to the dye emission centre and could show stronger lasing emission than  $\lambda_{SL}^I$  and  $\lambda_{SL}^{III}$ . Moreover, we could modify the available gain by changing dye concentration and also achieve tailored output behaviour of the different lasing modes (Supplementary Fig. 16 and Supplementary Movies 3 and 4). Such modular control over the input–output light curves of each lasing mode based on cavity resonances and gain can in principle lead to unique designs of multi-modal lasers.

Time-correlated photoluminescence (PL) measurements revealed distinct ultrafast decay dynamics of the different

superlattice lasing modes (Methods). Below the lasing threshold, PL from the IR-140-DMSO on NP superlattices exhibited an intrinsically long decay lifetime (834 ps) (Fig. 4a). Above threshold, the decay lifetime of photons from the dye can be significantly reduced by the faster process of stimulated emission<sup>7,9</sup> and modulated by the near-field distribution and mode quality of SL plasmons.  $\lambda_{SL}^a$  and  $\lambda_L$  showed the same in-phase NP oscillations in the near field, and we observed similar ultrashort decay lifetimes between  $\lambda_{SL}^I$  (16 ps) and  $\lambda_L^I$  (13 ps) (Fig. 4b,c). In contrast, the  $\lambda_{SL}^{II}$  lasing mode from patch–patch coupling exhibited a longer decay lifetime (41 ps) because photons could be trapped in the  $\lambda_{SL}^{b1}$  mode for a longer time ( $Q_{\lambda_{SL}^{b1}} > Q_{\lambda_L}$ ; Supplementary Fig. 14). Specifically,  $\lambda_{SL}^I$  emerged earlier (at 27 ps) than  $\lambda_{SL}^{II}$  (at 35 ps) in part because the stronger near field at  $\lambda_{SL}^I$  led to faster population inversion build-up for lasing;  $\lambda_{SL}^I$  also decayed faster since these  $\lambda_{SL}^I$  photons did not exhibit long cavity lifetimes through non-radiative decay from the metal NPs.



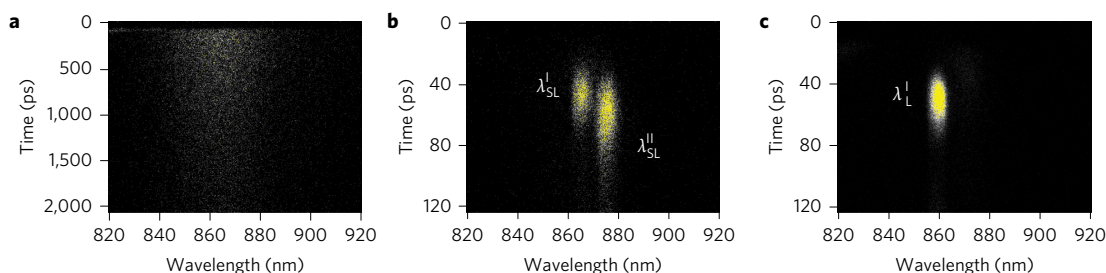


**Figure 4 | Modulation of the ultrafast decay dynamics of multi-modal lasing by micrometre patch-patch coupling.** **a–c**, Time-correlated single-photon counting of multi-modal lasing from NP superlattice arrays at  $0.03 \text{ mJ cm}^{-2}$  (**a**) and  $0.38 \text{ mJ cm}^{-2}$  (**b**), and single-lattice NP arrays at  $0.30 \text{ mJ cm}^{-2}$  (2 kHz, 800-nm femtosecond-pulsed laser; **c**). Only two lasing modes were observed at this pump power in **b** because of power-dependent multi-modal lasing.

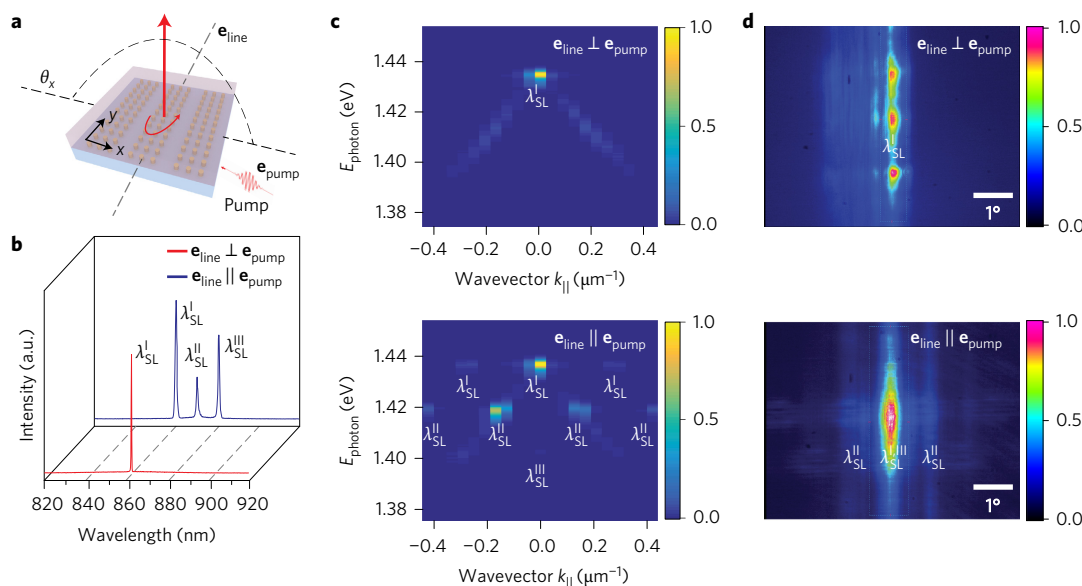


**Figure 5 | Dynamic control of band-edge modes in symmetry-broken plasmonic line patches leading to switchable nanolasing between single and multiple modes.** **a**, Schematic of the lasing measurement on NP line patches with the same  $a_0 = 600 \text{ nm}$ ,  $l = 18 \mu\text{m}$  and  $A_0 = 24 \mu\text{m}$  along  $x$  as in 2D superlattice arrays. **b**, Orientation-dependent lasing under TE polarization.  $\mathbf{e}_{\text{line}}$  and  $\mathbf{e}_{\text{pump}}$  represent the directions of line axis and pump polarization, respectively. **c**, Angle-resolved mapping of lasing emission by sweeping  $\theta_x$  with  $\mathbf{e}_{\text{line}} \perp \mathbf{e}_{\text{pump}}$  (top) and  $\mathbf{e}_{\text{line}} \parallel \mathbf{e}_{\text{pump}}$  (bottom). **d**, Far-field beam profiles from line patches under in-plane rotation of the sample. For  $\mathbf{e}_{\text{line}} \perp \mathbf{e}_{\text{pump}}$ , a single lasing mode at  $\lambda_{\text{SL}}^{\text{I}}$  produced multiple spots along  $y$  from patch-patch diffractive interference. For  $\mathbf{e}_{\text{line}} \parallel \mathbf{e}_{\text{pump}}$ , with pump power slightly above lasing threshold,  $\lambda_{\text{SL}}^{\text{III}}$  appeared in the middle while  $\lambda_{\text{SL}}^{\text{II}}$  showed up as two weak spots on the left and right. Intensity scale bars indicate normalized emitted photon intensity, increasing from blue to yellow or red.

Plasmonic superlattices can be fabricated with precise control over patch–patch spacing; hence, we can define the spectral location and spacing of the multiple lasing modes (Supplementary Fig. 17). As we increased  $A_0$  from 18 to 24 to 36  $\mu\text{m}$ , the spectral separation between band edges was reduced, as was the lasing modal spacing (from 14 to 11 to 7 nm, respectively, Supplementary Fig. 18). Consistent with Fig. 3a,  $\lambda_{\text{SL}}^{\text{II}}$  ( $k_{\parallel} \neq 0$ ) and  $\lambda_{\text{SL}}^{\text{III}}$  ( $k_{\parallel} = 0$ ) saturated at high pump powers while intensity at  $\lambda_{\text{SL}}^{\text{I}}$  ( $k_{\parallel} = 0$ ) continued to increase (Supplementary Fig. 19). The far-field spatial distribution of the different lasing modes could also be tailored by changing  $A_0$ . For example, at  $A_0 = 36 \mu\text{m}$ , multiple satellite spots over smaller detection angles ( $\theta_D = \pm 0.69^\circ$  at  $\lambda_{\text{SL}}^{\text{I}}$ ) were observed compared with that for  $A_0 = 24 \mu\text{m}$  ( $\theta_D = \pm 1.04^\circ$ ).

### Switchable lasing from symmetry-broken superlattices

Besides accurate spectral control of multiple nanolasing modes by tuning patch–patch spacing, we also spatially engineered band-edge modes with a symmetry-broken superlattice. We designed NP line patches with the same  $a_0$  and  $A_0$  as the 2D case (Fig. 1a) along  $x$ , while the structure along  $y$  only had a periodicity  $a_0$ , the same as the single-lattice array (Fig. 5a). Since plasmonic NPs

exhibit dipolar oscillations along the direction of incident light, symmetry-broken cavity structures enable polarization- and orientation-dependent band structures with either single or multiple band-edge modes (Supplementary Fig. 20). With pump polarization  $\mathbf{e}_{\text{pump}}$  along  $y$ , and line axis  $\mathbf{e}_{\text{line}}$  along  $x$  ( $\mathbf{e}_{\text{line}} \perp \mathbf{e}_{\text{pump}}$ ), we observed a single lasing mode at  $\lambda_{\text{SL}}^{\text{I}} = 862 \text{ nm}$  (Fig. 5b) from the single band-edge ( $k_{\parallel} = 0$ , Fig. 5c) and multiple spots along  $y$  from patch–patch diffractive interference. Conversely, when  $\mathbf{e}_{\text{line}} \parallel \mathbf{e}_{\text{pump}}$  (sample rotated in-plane), multiple lasing modes arose at  $\lambda_{\text{SL}}^{\text{I}} = 860 \text{ nm}$  ( $k_{\parallel} = 0$ ),  $\lambda_{\text{SL}}^{\text{II}} = 871 \text{ nm}$  ( $k_{\parallel} \neq 0$ ) and  $\lambda_{\text{SL}}^{\text{III}} = 881 \text{ nm}$  ( $k_{\parallel} = 0$ ) from the multiple band-edges. In the far field, these lasing modes were distributed along  $x$ , and no satellite spots appeared along  $y$  because there was no  $A_0$ ; the power-dependent output behaviour was similar to that of 2D superlattices (Supplementary Movie 5). As the sample was rotated in the  $x$ – $y$  plane, switchable nanolasing between single and multiple lasing modes (Supplementary Movie 6) agreed with the evolution of band structure from single to multiple band-edges (Supplementary Fig. 21).

The underlying mechanism of switchable lasing in the NP line patches can be attributed to the asymmetric spatial distribution of population inversion at the plasmonic hot spots. The four-level

model showed that population inversion accumulated only at dipolar hot spots along the pump polarization ( $y$ ) and increased faster when  $\mathbf{e}_{\text{line}} \perp \mathbf{e}_{\text{pump}}$  as a result of larger numbers of NPs coupling along  $x$  (Supplementary Fig. 22). Although dye molecules were randomly orientated and incoherent PL emission was independent of sample orientation, molecules with transition dipole moments along the pump polarization were preferentially excited; hence, the polarization of output lasing emission was along the polarization of the pump source (Supplementary Fig. 23). By fixing the sample orientation and changing the pump polarization, we also observed tunable lasing between single and multiple modes (Supplementary Fig. 24). Therefore, the lasing output can be dynamically manipulated in rationally designed NP superlattices.

## Conclusions

We demonstrated multi-modal nanolasing with controlled, large modal spacing from gold NP superlattices that support tunable, multiple band-edge modes at zero and non-zero wavevectors. Our model based on a four-level system coupled to FDTD calculations fully captures the multi-modal lasing contributions from zero and off-normal angles. Compared with conventional micro- and nanostructured lasers, multi-modal lasing from NP superlattices shows strikingly different output emission behaviour, spatial coherence and ultrafast decay dynamics characteristics. Notably, the relative ratios of the different modes can be tuned by changing NP size and local gain concentration. Coherent nanoscale light sources with well-controlled mode position, spacing and output characteristics can enable multiplexing for on-chip photonic devices and offer prospects for multi-modal laser designs. Moreover, engineering slow light at multiple band-edges is useful for manipulating strong light–matter interactions for lasing, optical nonlinearities, quantum optics, and other optical processes.

## Methods

Methods and any associated references are available in the [online version of the paper](#).

Received 19 September 2016; accepted 30 May 2017;  
published online 10 July 2017

## References

- Lopez, N., Reichertz, L. A., Yu, K. M., Campman, K. & Walukiewicz, W. Engineering the electronic band structure for multiband solar cells. *Phys. Rev. Lett.* **106**, 028701 (2011).
- Withers, F. *et al.* Light-emitting diodes by band-structure engineering in van der Waals heterostructures. *Nat. Mater.* **14**, 301–306 (2015).
- Qian, F. *et al.* Multi-quantum-well nanowire heterostructures for wavelength-controlled lasers. *Nat. Mater.* **7**, 701–706 (2008).
- Figotin, A. & Vitebskiy, I. Slow light in photonic crystals. *Waves Random Complex Media* **16**, 293–382 (2006).
- Painter, O. *et al.* Two-dimensional photonic band-gap defect mode laser. *Science* **284**, 1819–1821 (1999).
- Pickering, T., Hamm, J. M., Page, A. F., Wuestner, S. & Hess, O. Cavity-free plasmonic nanolasing enabled by dispersionless stopped light. *Nat. Commun.* **5**, 4972 (2014).
- Zhou, W. *et al.* Lasing action in strongly coupled plasmonic nanocavity arrays. *Nat. Nanotech.* **8**, 506–511 (2013).
- Schokker, A. H. & Koenderink, A. F. Lasing at the band edges of plasmonic lattices. *Phys. Rev. B* **90**, 155452 (2014).
- Yang, A. *et al.* Real-time tunable lasing from plasmonic nanocavity arrays. *Nat. Commun.* **6**, 6939 (2015).
- Yang, A. *et al.* Unidirectional lasing from template-stripped two-dimensional plasmonic crystals. *ACS Nano* **9**, 11582–11588 (2015).
- Zheludev, N. I., Prosvirnin, S. L., Papasimakis, N. & Fedotov, V. A. Lasing spaser. *Nat. Photon.* **2**, 351–354 (2008).
- Stockman, M. I. Spasers explained. *Nat. Photon.* **2**, 327–329 (2008).
- Bergman, D. J. & Stockman, M. I. Surface plasmon amplification by stimulated emission of radiation: quantum generation of coherent surface plasmons in nanosystems. *Phys. Rev. Lett.* **90**, 027402 (2003).
- Oulton, R. F. *et al.* Plasmon lasers at deep subwavelength scale. *Nature* **461**, 629–632 (2009).
- Ma, R. M., Oulton, R. F., Sorger, V. J., Bartal, G. & Zhang, X. Room-temperature sub-diffraction-limited plasmon laser by total internal reflection. *Nat. Mater.* **10**, 110–113 (2011).
- Lu, Y. J. *et al.* Plasmonic nanolaser using epitaxially grown silver film. *Science* **337**, 450–453 (2012).
- Hakala, T. K. *et al.* Lasing in dark and bright modes of a finite-sized plasmonic lattice. *Nat. Commun.* **8**, 13687 (2017).
- Turnbull, G. A., Andrew, P., Jory, M. J., Barnes, W. L. & Samuel, I. D. W. Relationship between photonic band structure and emission characteristics of a polymer distributed feedback laser. *Phys. Rev. B* **64**, 125122 (2001).
- Auguie, B. & Barnes, W. L. Collective resonances in gold nanoparticle arrays. *Phys. Rev. Lett.* **101**, 143902 (2008).
- Kravets, V. G., Schedin, F. & Grigorenko, A. N. Extremely narrow plasmon resonances based on diffraction coupling of localized plasmons in arrays of metallic nanoparticles. *Phys. Rev. Lett.* **101**, 087403 (2008).
- Zou, S., Janel, N. & Schatz, G. C. Silver nanoparticle array structures that produce remarkably narrow plasmon lineshapes. *J. Chem. Phys.* **120**, 10871–10875 (2004).
- Hill, M. T. & Gather, M. C. Advances in small lasers. *Nat. Photon.* **8**, 908–918 (2014).
- Fan, F., Turkdogan, S., Liu, Z., Shelhammer, D. & Ning, C. Z. A monolithic white laser. *Nat. Nanotech.* **10**, 796–803 (2015).
- Ma, R. M., Yin, X., Oulton, R. F., Sorger, V. J. & Zhang, X. Multiplexed and electrically modulated plasmon laser circuit. *Nano Lett.* **12**, 5396–5402 (2012).
- Henzie, J., Lee, M. H. & Odom, T. W. Multiscale patterning of plasmonic metamaterials. *Nat. Nanotech.* **2**, 549–554 (2007).
- Wang, D., Yang, A., Hryn, A. J., Schatz, G. C. & Odom, T. W. Superlattice plasmons in hierarchical Au nanoparticle arrays. *ACS Photon.* **2**, 1789–1794 (2015).
- Siegman, A. E. *Lasers* (University Science Books, 1986).
- Zhang, Q., Ha, S. T., Liu, X., Sum, T. C. & Xiong, Q. Room-temperature near-infrared high-Q perovskite whispering-gallery planar nanolasers. *Nano Lett.* **14**, 5995–6001 (2014).

## Acknowledgements

This work was supported by the National Science Foundation (NSF) under DMR-1608258 and DMR-1306514 (D.W., A.Y., W.W., G.C.S., T.W.O.). This work made use of the Northwestern University Micro/Nano Fabrication Facility (NUFAB), which is supported by the State of Illinois and Northwestern University. This work made use of the EPIC facility of the Northwestern University's Atomic and Nanoscale Characterization Experimental Center (NUANCE), which has received support from the Soft and Hybrid Nanotechnology Experimental (SHyNE) Resource (NSF NNCI-1542205); the MRSEC programme (NSF DMR-1121262) at the Materials Research Center; the International Institute for Nanotechnology (IIN); the Keck Foundation; and the State of Illinois, through the IIN. Use of the Center for Nanoscale Materials, an Office of Science user facility, was supported by the US Department of Energy, Office of Science, Office of Basic Energy Sciences, under contract no. DE-AC02-06CH11357. This research was supported in part by the Quest high performance computing facility at Northwestern University, which is jointly supported by the Office of the Provost, the Office for Research, and Northwestern University Information Technology.

## Author contributions

D.W. and T.W.O. conceived the idea of engineering the band-edge modes for nanolasing with plasmonic nanoparticle superlattices. D.W. fabricated the devices, carried out the optical measurements, and performed FDTD numerical simulations of the band structure, near-field distribution and multi-modal lasing actions of the system. D.W. and A.Y. carried out lasing measurements, and Y.H. set up the angle-resolved emission map equipment. D.W., W.W. and R.D.S. carried out TA measurements, and R.D.S. set up the equipment. T.W.O. and G.C.S. guided the experimental and theoretical investigations. D.W., G.C.S. and T.W.O. analysed the data and wrote the manuscript. All authors commented on and revised the manuscript.

## Additional information

Supplementary information is available in the [online version of the paper](#). Reprints and permissions information is available online at [www.nature.com/reprints](http://www.nature.com/reprints). Publisher's note: Springer Nature remains neutral with regard to jurisdictional claims in published maps and institutional affiliations. Correspondence and requests for materials should be addressed to G.C.S. and T.W.O.

## Competing financial interests

The authors declare no competing financial interests.

## Methods

**Fabrication of gold NP superlattices.** We fabricated gold NP superlattices with multiscale patterning<sup>26</sup> and compared their lasing properties with those of arrays with a single periodicity. Gold NP superlattices on glass were fabricated starting with a series of soft nanofabrication processes referred to as PEEL (photolithography, etching, electron-beam deposition and lift-off)<sup>29</sup>. Briefly, we first generated hierarchical photoresist posts on Si wafers after contact photolithography, Cr deposition, resist lift-off, and phase-shifting photolithography with a polydimethylsiloxane (PDMS) mask<sup>30</sup>. We used a 8-nm Cr layer as an isolation layer between contact and phase-shifting photolithography to create uniform photoresist posts within the patch. Hierarchical patterns of photoresist posts were then transferred into free-standing gold films of hierarchical nanohole arrays with PEEL. Finally, we created superlattices by gold deposition through the hole-array mask on glass substrates and then removal of the mask. Note that a 2-nm Cr layer was deposited before gold for better adhesion between gold NPs and the fused silica substrate. With multiscale patterning, the patch geometries ( $A_0$ ,  $l$ ) and NP spacings ( $a_0$ ) can be controlled independently by the flexible selection of Cr and PDMS masks, and the diameters of cylindrical NPs ( $d$ ) and height ( $h$ ) can be tuned by fabrication procedures of phase-shifting photolithography and metal deposition for hole-array mask.

**Lasing measurements.** Gold NP arrays embedded with gain IR-140-DMSO were pumped with a mode-locked Ti:sapphire laser with a regenerative amplifier laser (800 nm wavelength, 1 kHz repetition rate and 90 fs pulse width) at incident angle of 45°; the circular spot size was 2 mm in diameter (Supplementary Fig. 2). Lasing signals were collected normal to the sample surface and directed to a charge-coupled device (CCD) spectrometer (LN<sub>2</sub>-cooled CCD/Triax 552, Horiba Jobin Yvon, ~0.15 nm resolution). For angle-resolved emission measurements, we fixed the sample vertically at the centre of a rotational stage and collected emission signals within detection angle  $\theta_D = \pm 3.5^\circ$  in  $0.33^\circ$  increments manually (with respect to the sample surface normal). The collected signals were then directed to a compact spectrometer (USB 2000, Ocean Optics, 0.3 nm resolution) through an optical fibre. The far-field emission patterns of multi-modal lasing were analysed by a high-resolution CCD beam profiler (LBR-HR, Newport, 1.4 megapixel). By placing the beam profiler at different emission distances (4–6 cm) normal to the sample surface and a longpass filter (830 nm) in-between to filter the scattering light, we characterized the beam divergence of multiple lasing modes (Supplementary Fig. 8).

**Band structure measurements.** We placed the samples vertically at the centre of a program-controlled rotational stage and collected transmission spectra with various incident angles  $\theta_i$  swept in the  $x$ - $z$  plane<sup>26</sup>. Transmission spectra were collected from incident angles  $-3.5^\circ$  to  $3.5^\circ$  in  $0.2^\circ$  increments using an automated, home-built National Instruments Lab-VIEW program. Collimated, TE polarized white light from a halogen lamp (100 W) illuminated the sample with a spot size of 2 mm. The reflected light was coupled into a bundled optical fibre connected to a Princeton Instruments Acton SpectraPro2500 spectrometer with a PIXIS:400 CCD detector. Band structures of the single-lattice and superlattice arrays in wavelength ( $\lambda$ )– and incident angle ( $\theta_i$ ) units were constructed by stitching together a series of angle-resolved transmission spectra and then transferred to energy ( $E$ )– and wavevector ( $k_{||}$ ) units by  $E = hc/\lambda$  and  $k_{||} = (2\pi/\lambda) \sin\theta_i$ .

**Time-resolved photoluminescence (PL).** A streak camera was used to characterize fluence-dependent, wavelength-resolved PL decay experiments and to characterize different multiple lasing modes. A 2-kHz amplified Ti:sapphire laser operating at

800 nm excited the samples at an incident angle  $\theta_i = 75^\circ$ . The PL signals were passed through 830-nm longpass and neutral density filters and then coupled to a fibre optic on a rotational stage with samples placed at the circular centre. Fibre-coupled photons were directed to a 0.15 m grating spectrometer, dispersed with a 150-groove per mm grating, and detected with a single-photon-sensitive streak camera. The emission decay lifetime,  $t$ , was obtained from fitting the collected data with an exponential decay function  $y = y_0 + Ae^{-(x-x_0)/t}$ .

**FDTD simulations of band structures and multi-modal nanolasing.** FDTD calculations with commercial software (FDTD solution, Lumerical Inc.) were used to simulate the linear properties of gold NPs. The optical constants of gold were taken from ref. 31 (400–1,000 nm). A uniform mesh size of 4 nm ( $x$ ,  $y$  and  $z$ ) was used to ensure accuracy of electric and magnetic field calculations within the metal NPs.

Simulation of multi-modal lasing was performed by the same software (FDTD Solutions, Lumerical Inc.), where a four-level one-electron model was integrated with FDTD for modelling dye molecules and the only available model included the Pauli exclusion principle. (Details of the model and parameters are provided in Supplementary Fig. 9.) As a test case, we used a superlattice design with patch periodicity  $A_0 = 24 \mu\text{m}$  and patch length  $l = 18 \mu\text{m}$ . In the four-level systems, we set the NP size  $d$  as 120 nm and 125 nm, dye concentration  $C = 1 \text{ mM}$ , pump wavelength at  $\lambda_a = 800 \text{ nm}$  and dye emission at  $\lambda_e = 860 \text{ nm}$  with bandwidth  $\Delta\lambda_e = 100 \text{ nm}$ , which is close to experimental conditions. Initially, we pumped the four-level system from the ground state (population density  $N_0 = 1$ ,  $N_1 = N_2 = N_3 = 0$ ) and collected all emitted flux with a plane monitor placed  $0.3 \mu\text{m}$  away on top of the NPs. A more sophisticated treatment of the dye molecules that would include for mode coupling and mode competition is beyond the scope of our current four-level model. However, the non-radiative dephasing rate  $\tau_c$  in our oscillator equation

$$\frac{d^2 \mathbf{P}_e}{dt^2} + \tau_c \frac{d\mathbf{P}_e}{dt} + \omega_c^2 \mathbf{P}_e = k_e (N_2 - N_1) \mathbf{E}$$

where  $\mathbf{P}_e$  is the net macroscopic polarization and  $k_e$  is the oscillation parameter introduces broadening of the radiative emission linewidth, which allows for lasing (including multi-modal lasing) over a range of wavelengths. By integrating the NP superlattices with the commercial software, we increased the computation efficiency dramatically compared with a previously developed home-built FDTD code in Matlab<sup>7</sup>. Moreover, we could characterize off-normal emission at non-zero  $k_{||}$  by introducing a phase shift at the unit boundary with Bloch boundary conditions, which is not feasible in the home-built code.

**Data availability.** The data that support the plots within this paper and other findings of this study are available from the corresponding author upon reasonable request.

## References

- Gao, H., Henzie, J. & Odom, T. W. Direct evidence for surface plasmon-mediated enhanced light transmission through metallic nanohole arrays. *Nano Lett.* **6**, 2104–2108 (2006).
- Odom, T. W., Love, J. C., Wolfe, D. B., Paul, K. E. & Whitesides, G. M. Improved pattern transfer in soft lithography using composite stamps. *Langmuir* **18**, 5314–5320 (2002).
- Johnson, P. B. & Christy, R. W. Optical constants of noble metals. *Phys. Rev. B* **6**, 4370–4379 (1972).